

## Article

---

# Partition Function Zeros of the Frustrated $J_1-J_2$ Ising Model on the Honeycomb Lattice

---

Denis Gessert, Martin Weigel and Wolfhard Janke

## Special Issue

Violations of Hyperscaling in Phase Transitions and Critical Phenomena—in Memory of Prof. Ralph Kenna

Edited by

Prof. Bertrand Berche and Prof. Yurij Holovatch

## Article

# Partition Function Zeros of the Frustrated $J_1$ - $J_2$ Ising Model on the Honeycomb Lattice

Denis Gessert <sup>1,2</sup> , Martin Weigel <sup>3,\*</sup>  and Wolfhard Janke <sup>1</sup> <sup>1</sup> Institut für Theoretische Physik, Leipzig University, IPF 231101, 04081 Leipzig, Germany; denis.gessert@itp.uni-leipzig.de (D.G.); wolfhard.janke@itp.uni-leipzig.de (W.J.)<sup>2</sup> Centre for Fluid and Complex Systems, Coventry University, Coventry CV1 5FB, UK; gessertd@uni.coventry.ac.uk<sup>3</sup> Institut für Physik, Technische Universität Chemnitz, 09107 Chemnitz, Germany

\* Correspondence: martin.weigel@physik.tu-chemnitz.de

**Abstract:** We study the zeros of the partition function in the complex temperature plane (Fisher zeros) and in the complex external field plane (Lee–Yang zeros) of a frustrated Ising model with competing nearest-neighbor ( $J_1 > 0$ ) and next-nearest-neighbor ( $J_2 < 0$ ) interactions on the honeycomb lattice. We consider the finite-size scaling (FSS) of the leading Fisher and Lee–Yang zeros as determined from a cumulant method and compare it to a traditional scaling analysis based on the logarithmic derivative of the magnetization  $\partial \ln \langle |M| \rangle / \partial \beta$  and the magnetic susceptibility  $\chi$ . While for this model both FSS approaches are subject to strong corrections to scaling induced by the frustration, their behavior is rather different, in particular as the ratio  $\mathcal{R} = J_2/J_1$  is varied. As a consequence, an analysis of the scaling of partition function zeros turns out to be a useful complement to a more traditional FSS analysis. For the cumulant method, we also study the convergence as a function of cumulant order, providing suggestions for practical implementations. The scaling of the zeros convincingly shows that the system remains in the Ising universality class for  $\mathcal{R}$  as low as  $-0.22$ , where results from traditional FSS using the same simulation data are less conclusive. Hence, the approach provides a valuable additional tool for mapping out the phase diagram of models afflicted by strong corrections to scaling.



**Citation:** Gessert, D.; Weigel, M.; Janke, W. Partition Function Zeros of the Frustrated  $J_1$ - $J_2$  Ising Model on the Honeycomb Lattice. *Entropy* **2024**, *26*, 919. <https://doi.org/10.3390/e26110919>

Academic Editor: Antonio M. Scarfone

Received: 2 October 2024

Revised: 14 October 2024

Accepted: 15 October 2024

Published: 29 October 2024



**Copyright:** © 2024 by the authors. Licensee MDPI, Basel, Switzerland. This article is an open access article distributed under the terms and conditions of the Creative Commons Attribution (CC BY) license (<https://creativecommons.org/licenses/by/4.0/>).

## 1. Introduction

Frustrated systems [1] are characterized by interactions that cannot all be satisfied simultaneously. The resulting internal competition leads to quite interesting critical properties such as re-entrant phase behavior [2] and non-zero ground state entropy [3,4]. One of the most well-studied systems in this class is the Ising model with competing first- and second-neighbor interactions on the square lattice [5–9]. Noting that in the presence of frustration the lattice geometry is of fundamental importance for the occurrence and symmetry of ordered phases, it is somewhat surprising that much less is known about the analogous system on the honeycomb lattice, which only recently started to attract some attention [10–13]. Depending on the ratio  $\mathcal{R}$  of the next-nearest-neighbor and nearest-neighbor interaction strengths, the system has a ferromagnetic ground state for  $\mathcal{R} > -1/4$  or a largely degenerate ground state of known energy for  $\mathcal{R} < -1/4$  [10]. The understanding of the critical properties for  $\mathcal{R} \lesssim -0.2$  remains limited. Here, we focus on  $\mathcal{R} > -1/4$ , for which the system remains ferromagnetic at zero temperature.

Metastable states are a common feature in frustrated systems and their presence is a challenge for standard simulation techniques since runs become trapped in local minima. Particularly difficult are systems with rugged free-energy landscapes [14]. One contender among generalized-ensemble simulation techniques suitable for such problems is population annealing (PA) [15,16], which has recently shown its versatility in a range of

applications [17–19]. PA is particularly well suited for studying such systems with many competing minima, as the large number of replicas allows sampling many local minima simultaneously. This is in contrast to its one-replica counterpart, equilibrium simulated annealing [20], which is much more likely to become trapped in a single local minimum and, hence, to fail to sample the equilibrium distribution.

Systems with competing interactions often are subject to strong corrections to scaling (commonly of unknown shape). For the above-mentioned frustrated Ising model on the square lattice, for example, which has been discussed since the 1970s [5], the study of the tricritical point required simulations of rather large system sizes, but notwithstanding this effort certain aspects remain unclear [6–9].

An alternate approach for studying phase transitions revolves around considering zeros of the partition function in the complex external field and temperature planes, based on the pioneering work by Lee and Yang [21,22] and by Fisher [23]. Using these zeros allows one to distinguish between first- and second-order transitions as well as to extract estimates of their strengths [24–27], and to examine the peculiar properties of a model with special boundary conditions [28,29]. The cumulative density of zeros and their impact angle onto the real temperature axis encode the strength of higher-order phase transitions [30–34]. This can also be used as a medium for deriving scaling relations among logarithmic correction exponents [35,36]. For a recent discussion along an alternative route, see Ref. [37].

For non-frustrated systems, the scaling of partition function zeros has been shown to yield quite accurate results for critical exponents, even when using rather small system sizes [38,39], suggesting that this might also be the case for more complex systems. Previous work studying partition function zeros for frustrated spin systems includes Refs. [40–43].

Despite some experimental measurements of zeros in complex external magnetic fields [44–46], the most established approach of studying complex partition function zeros requires an accurate estimate of the full density of states, which is difficult to obtain both in experiments as well as in simulations (but see Ref. [47]). For simulations, this commonly limits the maximum system size that can be studied. More recently, an alternative method for obtaining the leading partition function zero based on cumulants of the energy and magnetization distributions has gained some traction [48], thus enabling determinations of partition function zeros from more easily accessible observables in simulations. We use this method to analyze the finite-size scaling (FSS) of the zeros for system sizes exceeding those for which we could determine the full density of states.

For the frustrated Ising model on the honeycomb lattice, initial work using effective field theory (EFT) [10] suggested the existence of a tricritical point near  $\mathcal{R} \approx -0.1$ . This was later challenged through a Monte Carlo study [12], showing that the system remains within the Ising universality class at least down to  $\mathcal{R} = -0.2$ . Cluster mean-field theory [13] suggests that the transition may remain of second order down to  $\mathcal{R} = -1/4$ , but this has not been verified in the actual model. With this paper, we aim at a better understanding of the critical properties of this system, particularly close to the special point  $\mathcal{R} = -1/4$ , at which the critical temperature vanishes. To this end, we consider the scaling of the partition function zeros.

## 2. Materials and Methods

### 2.1. Model

We study the well-known two-dimensional Ising model, but placed on the honeycomb lattice and equipped with competing nearest- and next-nearest-neighbor interactions, resulting in the Hamiltonian

$$\mathcal{H} = -J_1 \sum_{\langle ij \rangle} \sigma_i \sigma_j - J_2 \sum_{[ik]} \sigma_i \sigma_k - h \sum_i \sigma_i \equiv -J_1 \Sigma_1 - J_2 \Sigma_2 - h M, \quad (1)$$

where  $\langle ij \rangle$  and  $[ik]$  denote sums over nearest neighbors and next-nearest neighbors, respectively,  $J_1 > 0$  is the ferromagnetic nearest-neighbor interaction strength,  $J_2 < 0$  is the competing antiferromagnetic next-nearest-neighbor interaction strength, and  $h$  the mag-

netic field.  $\Sigma_1$  and  $\Sigma_2$  refer to the sums over nearest- and next-nearest-neighbor interactions, respectively, and  $M$  is the (total) magnetization. The quantity relevant for the nature of the ordered phase and the transition is the ratio  $\mathcal{R} = J_2/J_1$  of couplings. Here, we only consider the case of  $\mathcal{R} \in (-1/4, 0]$ , where the ground state is ferromagnetic [10]. We study systems of linear lattice size  $L$ , which due to the two-atom basis of the honeycomb lattice contain  $N = 2L^2$  spins. Note that all simulations were carried out in the absence of an external magnetic field. We include the magnetic term here as it is necessary for the discussion of the Lee–Yang zeros.

## 2.2. Partition Function Zeros

In terms of the density of states  $\Omega(\Sigma_1, \Sigma_2, M)$ , the partition function at inverse temperature  $\beta$  and external magnetic field  $h$  is given by

$$\mathcal{Z}(\beta, h) = \sum_{\Sigma_1} \sum_{\Sigma_2} \sum_M \Omega(\Sigma_1, \Sigma_2, M) e^{\beta J_1 \Sigma_1 + \beta J_2 \Sigma_2 + \beta h M}. \quad (2)$$

We choose both  $J_1$  and  $J_2$  to be integers, such that for  $h = 0$  the partition function is a polynomial in  $x = e^{-\beta}$ . For  $h \neq 0$ , on the other hand, the partition function may be written as a polynomial in  $e^{2\beta h}$  for arbitrary choices of  $J_1$  and  $J_2$ . The complex inverse temperatures  $\{\beta_k\}$  solving the equation  $\mathcal{Z}(\beta = \beta_k, h = 0) = 0$ , i.e., in the absence of an external magnetic field  $h$ , are called Fisher zeros. Once calculated, the Fisher zeros will be studied as a function of  $z = x^{J_1}$  to allow for better comparability of the results for different values of  $\mathcal{R} = J_2/J_1$ . Note that, as is well known, different variables yield very different visual impressions for the locations of zeros (see, for example, Appendix A). The pair of zeros closest to the positive real axis approaches  $(\beta_c, 0) = \beta_c + 0i$  as  $L \rightarrow \infty$ . The real and imaginary parts of these leading zeros  $\beta_0$  usually scale as [49]

$$\Re(\beta_0) - \beta_c \propto L^{-y_t}, \quad (3)$$

and

$$\Im(\beta_0) \propto L^{-y_t}, \quad (4)$$

respectively, with  $y_t$  being the renormalization group (RG) eigenvalue related to the temperature variable, which is connected to the critical exponent of the correlation length by  $y_t = 1/\nu$ .

The complex magnetic fields  $\{h_k\}$  that solve the equation  $\mathcal{Z}(\beta, h = h_k) = 0$  for some fixed  $\beta$  are the so-called Lee–Yang zeros that lie on the unit circle  $e^{2\beta h} = e^{i\varphi}$  for the Ising ferromagnet, implying that all solutions for  $h_k$  are purely imaginary [21,22]. This circle theorem has been extended to many more models [50], but it is not universally valid, see, e.g., Refs. [51,52]. For the Ising model with competing interactions placed on a square lattice, the circle law was found to apply in the regime with ferromagnetic ground state [53]. As  $L \rightarrow \infty$ , the Lee–Yang zeros closest to the positive real axis approach zero. At the inverse critical temperature  $\beta_c$ , the imaginary part of the leading zeros  $h_0$  scales as [49]

$$\Im(h_0) \propto L^{-y_h}, \quad (5)$$

with  $y_h$  being the RG eigenvalue related to the external magnetic field, which is connected to the standard critical exponents by  $y_h = (\beta + \gamma)/\nu$ .

To numerically estimate partition function zeros, writing  $\beta = \Re(\beta) + i\Im(\beta)$  one notes that for zero field,  $h = 0$ , the Fisher zeros of  $\mathcal{Z}(\beta, h = 0)$  are identical to the zeros of

$$\begin{aligned} \mathcal{Z}(\Re(\beta), \Im(\beta)) &\equiv \frac{\mathcal{Z}(\Re(\beta) + i\Im(\beta), h = 0)}{\mathcal{Z}(\Re(\beta), h = 0)} \\ &= \langle \cos(\Im(\beta)\mathcal{H}) \rangle_{\Re(\beta), h=0} - i \langle \sin(\Im(\beta)\mathcal{H}) \rangle_{\Re(\beta), h=0}, \end{aligned} \quad (6)$$

and likewise the Lee–Yang zeros for fixed (real)  $\beta$  might be extracted from

$$\begin{aligned} Z_\beta(\Re(h), \Im(h)) &\equiv \frac{\mathcal{Z}(\beta, \Re(h) + i\Im(h))}{\mathcal{Z}(\beta, \Re(h))} \\ &= \langle \cos(\Im(h)M) \rangle_{\beta, \Re(h)} - i \langle \sin(\Im(h)M) \rangle_{\beta, \Re(h)}. \end{aligned} \quad (7)$$

While the evaluation of (6) and (7) and a systematic search for zeros requires the availability of the density of states  $\Omega$  for reweighting [39,54–56], more recently a computationally lighter method based on cumulants of thermodynamic observables  $\Phi(q)$ , i.e.,

$$\langle\langle \Phi^n(q) \rangle\rangle = \frac{\partial^n}{\partial q^n} \ln \mathcal{Z}(q) \quad (8)$$

has been suggested [38,48,57–59]. Here, the notation  $\Phi(q)$  refers to the thermodynamic observables  $\mathcal{H}$  and  $M$  as a function of their control parameters  $q = -\beta$  and  $q = \beta h$ , respectively, unifying the discussion of Fisher and Lee–Yang zeros. The method relies on the fact that the partition function can be factorized in a regular (non-zero) part  $\tilde{\mathcal{Z}}(q) = \mathcal{Z}(0)e^{cq}$  for some constant  $c$  and the product of its complex roots in  $q$ , i.e.,

$$\mathcal{Z}(q) = \tilde{\mathcal{Z}}(q) \prod_k (1 - q/q_k). \quad (9)$$

Note that by Equation (2)  $\mathcal{Z}(q)$  is real for real  $q$ , and that thus the roots  $q_k$  in (9) appear in complex conjugate pairs. Plugging (9) into (8) yields the expression

$$\langle\langle \Phi^n(q) \rangle\rangle = - \sum_k \frac{(n-1)!}{(q_k - q)^n}, \quad n > 1 \quad (10)$$

for the cumulants. The key point of the method is that the contribution of non-leading zeros in the expression above is suppressed by powers of  $n$  for the  $n$ -th order cumulant. Thus, one neglects the non-leading zeros, which allows the calculation of the leading partition function zeros using only the first few cumulants of the energy and magnetization,  $\langle\langle \mathcal{H}^n \rangle\rangle$  and  $\langle\langle M^n \rangle\rangle$ , and hence does not require knowledge of  $\Omega$ . Cumulants can be calculated from the central moments,  $\langle\Phi^n\rangle_c = \langle(\Phi - \langle\Phi\rangle)^n\rangle$ . The first four cumulants are given by

$$\langle\langle \Phi \rangle\rangle = \langle\Phi\rangle, \quad \langle\langle \Phi^2 \rangle\rangle = \langle\Phi^2\rangle_c, \quad \langle\langle \Phi^3 \rangle\rangle = \langle\Phi^3\rangle_c, \quad \langle\langle \Phi^4 \rangle\rangle = \langle\Phi^4\rangle_c - 3\left(\langle\Phi^2\rangle_c\right)^2. \quad (11)$$

Relations for higher-order cumulants can be found using computer algebra systems. (We use the MATHEMATICA function `MomentConvert` to obtain the relations up to the 20-th cumulant. The first ten cumulants are listed in Ref. [60].) Within this framework, the leading zeros  $q_0$  can be extracted in a vector-matrix notation from [48]

$$\begin{pmatrix} 2 \Re(q_0 - q) \\ |q_0 - q|^2 \end{pmatrix} \approx \begin{pmatrix} 1 & -\frac{\mu_n^{(+)}}{n} \\ 1 & -\frac{\mu_{n+1}^{(+)}}{n+1} \end{pmatrix}^{-1} \begin{pmatrix} (n-1)\mu_n^{(-)} \\ n\mu_{n+1}^{(-)} \end{pmatrix}, \quad (12)$$

where  $n$  is the approximation order, and  $\mu_n^{(\pm)}$  denotes the ratio of two cumulants of consecutive orders, i.e.,  $\mu_n^{(\pm)} \equiv \langle\langle \Phi^{n\pm 1} \rangle\rangle / \langle\langle \Phi^n \rangle\rangle$ .  $(\Phi, q) = (E, -\beta)$  corresponds to Fisher zeros, and  $(\Phi, q) = (M, \beta h)$  to Lee–Yang zeros. Since odd cumulants of  $M$  vanish for  $h = 0$ , when setting  $n = 2k$  the expression for the Lee–Yang zeros simplifies to [39,59]

$$\Im(h_0) \approx \pm \frac{1}{\beta} \sqrt{2k(2k+1) \left| \frac{\langle\langle M^{2k}(0) \rangle\rangle}{\langle\langle M^{2(k+1)}(0) \rangle\rangle} \right|}. \quad (13)$$

### 2.3. Population Annealing

Population annealing (PA) [15,16] is a simulation scheme designed for parallel calculations for systems with complex free-energy landscapes in which the state space is sampled by a population of replicas that are cooled down collectively. It consists of alternating resampling and spin-update steps. As the temperature is lowered, the population is resampled according to the Boltzmann distribution at the new temperature [61]. Spin updates then help to equilibrate the replicas at this temperature, and to increase the diversity of the population [62]. The implementation of PA as used here can be summarized as follows:

1. Initialize the population by drawing  $R_0 = R$  random spin configurations corresponding to the initial inverse temperature  $\beta_0^{\text{PA}} = 0$ .
2. Set the iteration counter  $i \leftarrow 0$ .
3. Determine the next inverse temperature  $\beta_{i+1}^{\text{PA}}$  such that the energy histogram overlap between  $\beta_i^{\text{PA}}$  and  $\beta_{i+1}^{\text{PA}}$ , given by [63]

$$\alpha(\beta_i^{\text{PA}}, \beta_{i+1}^{\text{PA}}) = \frac{1}{R_i} \sum_{j=1}^{R_i} \min \left( 1, \frac{R e^{-(\beta_{i+1}^{\text{PA}} - \beta_i^{\text{PA}}) E_j}}{\sum_{k=1}^{R_i} e^{-(\beta_{i+1}^{\text{PA}} - \beta_i^{\text{PA}}) E_k}} \right), \quad (14)$$

is approximately equal to the target value of  $\alpha^*$ , where  $E_j$  refers to the current energy of replica  $j$ .

4. Increment  $i$  by 1.
5. Resample the replicas according to their relative Boltzmann weights, that is, make on average

$$\tau(E_j) = \frac{R e^{-(\beta_{i+1}^{\text{PA}} - \beta_i^{\text{PA}}) E_j}}{\sum_{k=1}^{R_i} e^{-(\beta_{i+1}^{\text{PA}} - \beta_i^{\text{PA}}) E_k}} \quad (15)$$

copies of replica  $j$  with energy  $E_j$ .

6. Carry out Metropolis updates on the replicas until the effective population size  $R_{\text{eff}}$  (see [62] for definition and discussion) exceeds the threshold value of  $R^* = \rho^* R$ .
7. Calculate estimates for observables  $\mathcal{O}$  as the population averages  $\sum_j \mathcal{O}_j / R_i$ , where  $\mathcal{O}_j$  is the value of the observable for the  $j$ -th replica. Note that we calculate central moments of the energy directly during the simulation after calculating the average energy, because using raw moments to calculate higher-order central moments and cumulants leads to a complete loss of numeric precision in the latter.
8. Unless the lowest temperature of interest is reached, go to step 3.

Some comments are in order at this point. The above implementation contains numerous parameters of relevance to the performance of the algorithm, namely, the population size  $R$ , the target energy distribution overlap  $\alpha^*$ , and the sweep schedule given by the threshold value  $\rho^*$  for the relative effective population size. These have been (resp. will be) discussed elsewhere [61,62,64], and here we choose  $R = 20,000$  throughout,  $\alpha^*$  is set to at least 80%, in some cases 90%, and  $\rho^* \geq 90\%$ . There are in fact many possibilities of how the resampling step can be realized. Here, we use the so-called nearest-integer resampling which has been shown to lead to optimal results in many scenarios [61]. For the spin updates we employ the Metropolis method implemented on a GPU, drawing on a domain decomposition [63] into four sublattices, adapting and extending the publicly available code of Ref. [63]. For small system sizes, we obtain an estimate for the density of states by using multi-histogram reweighting, also implemented in the source code of Ref. [63].

## 3. Results

### 3.1. Solving for all Fisher Zeros in the Complex Temperature Plane

For finite systems, the partition function for  $h = 0$  is a polynomial of finite order in  $x = e^{-\beta}$  (for suitable choices of  $J_1$  and  $J_2$ ). In principle, once the density of states  $\Omega(E)$  is known one can solve for all partition function zeros numerically. Due to the presence of both  $J_1 \Sigma_1$  and  $J_2 \Sigma_2$  in the Hamiltonian, there are more than the usual  $\mathcal{O}(N)$  distinct

energy levels, namely up to  $\mathcal{O}(N^2)$  levels, where  $N = 2L^2$  is the number of spins in the honeycomb system. Thus, it is only feasible to calculate all partition function zeros for very small system sizes.

This is illustrated in Figure 1, where all Fisher zeros of a 32-spin system ( $L = 4$ ) with periodic boundary conditions for different values of  $\mathcal{R}$  are depicted. To compute the density of states we used exact enumeration of all possible  $2^{32}$  spin configurations. In the absence of next-nearest-neighbor interactions (i.e., for the standard ferromagnetic Ising case), the model can be solved analytically for  $L \rightarrow \infty$ ; see Appendix A for a comparison of the partition function zeros for  $L = 4$  with the exact solution in the thermodynamic limit. For  $\mathcal{R} = 0$ , the partition function is an even polynomial in  $z = x^{J_1}$ , and hence symmetric in  $z$ . This symmetry is broken by the introduction of the next-nearest-neighbor interactions, which is reflected in the asymmetry with respect to the ordinate axis in Figure 1, that becomes stronger with increasing  $|\mathcal{R}|$  (left to right). Also note that the number of zeros for the finite system size is much larger than for  $\mathcal{R} = 0$ . This is due to a smaller number of distinct energy levels for  $\mathcal{R} = 0$ , or in other words, the larger degeneracy of the individual energy levels. For  $L = 4$ , the Fisher zeros at  $z = \pm i$  for  $\mathcal{R} = 0$  each split into 16 distinct ones when  $|\mathcal{R}|$  is increased, and spread out as  $|\mathcal{R}|$  is increased further. For  $\mathcal{R} = -0.1$  this is well seen through the dense set of zeros near  $z = \pm i$ . For a better visual impression of how the Fisher zeros move as  $\mathcal{R}$  is changed, we refer to the Supplementary Materials, which contain an animation (video) illustrating the motion of Fisher zeros as  $\mathcal{R}$  is varied from 0 to  $-1$ , illustrating the splitting of the zero located at  $z = \pm i$  for  $\mathcal{R} = 0$  very clearly.

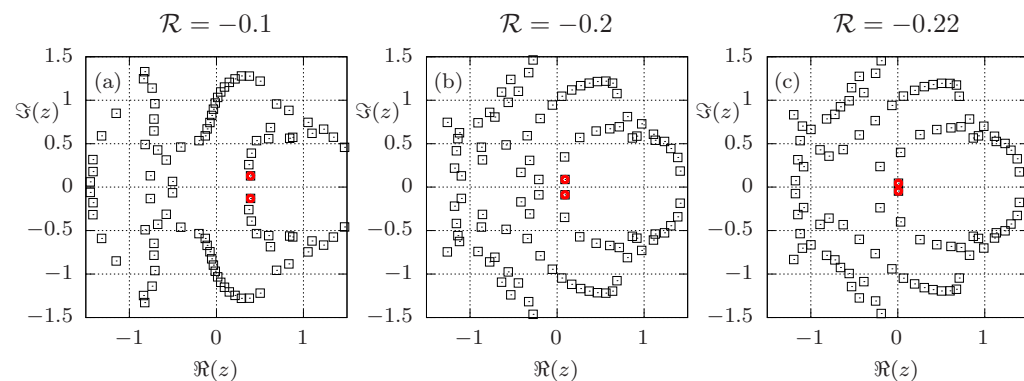


**Figure 1.** Fisher zeros in the (transformed) complex temperature  $z = e^{-\beta J_1}$  plane for  $L = 4$  and (a)  $\mathcal{R} = -0.1$ , (b)  $\mathcal{R} = -0.2$ , and (c)  $\mathcal{R} = -0.22$ . The red circles highlight the Fisher zeros closest to the positive real axis. Note that MATHEMATICA fails to find some zeros close to the real axis, which becomes apparent as some zeros that are visible for  $\mathcal{R} = -0.1$  and  $-0.2$  are absent for  $\mathcal{R} = -0.22$ .

From earlier studies [10,12], it is known that the critical temperature in this model approaches zero as  $\mathcal{R}$  goes to  $-1/4$ . This is reflected in Figure 1 by the leading Fisher zero (red circle) moving closer to the origin in this limit. Due to the small system size, the leading Fisher zero for  $\mathcal{R} = -0.22$  is very close to the imaginary axis. In fact, for  $\mathcal{R} \lesssim -0.222$ , the imaginary part of the leading Fisher zero in the  $\beta$ -plane,  $\Im(\beta_0)$ , exceeds  $\pi/2$ . Thus, in the  $z$ -plane the zero may lie in the region of negative real values for smaller values of  $\mathcal{R}$ . As  $\mathcal{R}$  approaches  $-1/4$ , both the real and imaginary part of  $\beta_0$  go to infinity. Thus, in the  $z$ -plane, the Fisher zero rotates around the origin as  $\mathcal{R}$  goes to  $-1/4$ . Since the imaginary part of  $\beta_0$  vanishes with increasing  $L$ , we understand this effect as a peculiar finite-size effect and expect it not to be relevant in the thermodynamic limit.

### 3.2. Determining the Leading Fisher Zero Directly and by the Cumulant Method

In the following, we verify the efficacy of the cumulant method developed by Flindt and Garrahan [48] by comparing its results to the estimates from reweighting for system sizes for which we obtained the density of states. As we were unable to calculate all partition function zeros for  $L > 4$ , we fall back to obtaining the value of the leading Fisher

zero used for comparison by numerically reweighting  $Z(\Re(\beta), \Im(\beta))$ . Except for  $L = 4$ , where exact enumeration was used, we estimate the density of states  $\Omega(\Sigma_1, \Sigma_2)$  by using multi-histogram reweighting (MHR) of our PA data [63]. (Note that we only measured the two-dimensional (energetic) density of states. Therefore, we do not have access to magnetic quantities and the Lee–Yang zeros.)

The top row of Figure 2 shows the absolute value of the partition function  $Z(\Re(\beta), \Im(\beta))$  in the complex  $\beta$ -plane as obtained from Equation (6) and for different values of  $\mathcal{R}$ , zoomed-in and centered around the leading Fisher zero for  $L = 4$  with positive imaginary part (using the same data as above). The open black circles denote the respective Fisher zero  $\beta_0^{(d)}$  found using the Levenberg–Marquardt (LM) algorithm [65,66], with an initial guess for  $\beta_0^{(d)}$  close to the root. (We use SCIPY’s `optimize.root` function to find the zeros with the parameter `method='lm'`, corresponding to the Levenberg–Marquardt algorithm.) In the following, we refer to this approach using the LM algorithm as the “direct method”. Note the added superscript (d) for the value of the leading Fisher zero obtained with this method. A commonly used alternative approach is to use one-dimensional root finding to determine the zeros of the real and imaginary parts of Equations (6) or (7) independently over a range of complex  $\beta$ ’s or  $h$ ’s, respectively, and then, to find their intersection, a method used, e.g., in Refs. [39,54–56].

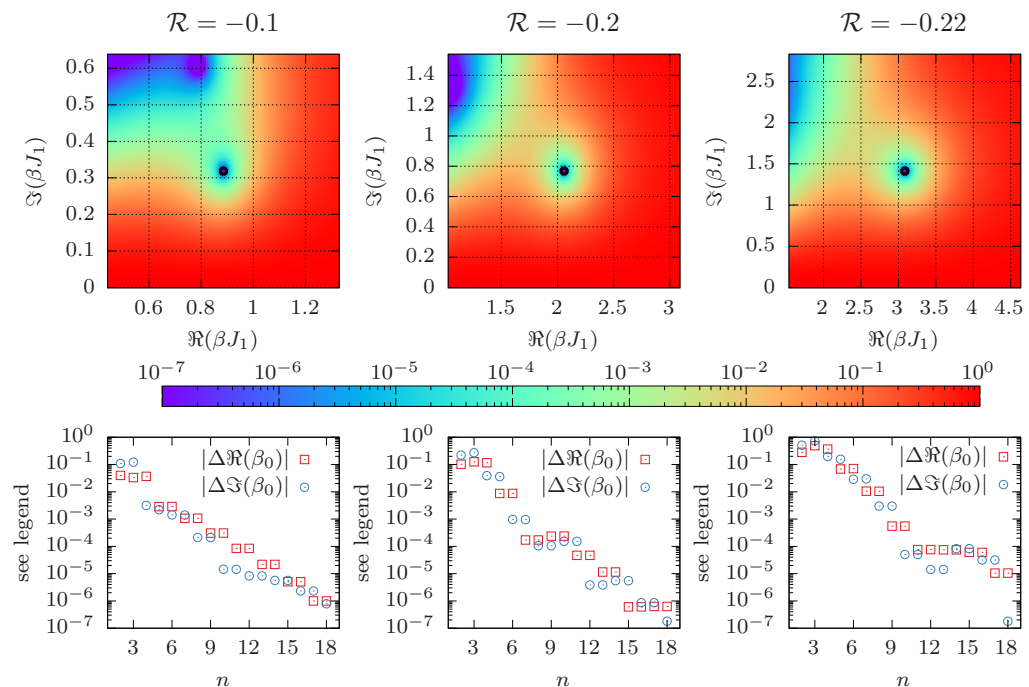


**Figure 2.** The top row shows heat maps of  $|Z(\Re(\beta), \Im(\beta))|$  for complex  $\beta$  as obtained from Equation (6) for  $\mathcal{R} \in \{-0.1, -0.2, -0.22\}$ , computed by exact enumeration for  $L = 4$ . The leading Fisher zero calculated by the direct method is denoted by an open black circle. The bottom row shows the differences  $\Delta\Re(\beta_0)$  and  $\Delta\Im(\beta_0)$  (see text for definitions), comparing the direct method with the cumulant method.

For the cumulant method, when the  $n$ -th order cumulants are evaluated at  $\beta = \Re(\beta_0^{(d)})$  the estimate for  $\Re(\beta - \beta_0)$  goes to zero with increasing  $n$  and the approximation of  $|\beta - \beta_0|^2$  approaches  $\Im(\beta_0^{(d)})^2$ . In principle, one can use any simulation point  $\beta$  and obtain estimates for the location of the Fisher zero. However, most precise results are found for  $\beta \approx \Re(\beta_0)$ . Thus, we can consider  $\Delta\Re(\beta_0) \equiv \Re(\beta - \beta_0)|_{n, \beta = \Re(\beta_0^{(d)})}$  and  $\Delta\Im(\beta_0) \equiv \sqrt{|\beta - \beta_0|^2}|_{n, \beta = \Re(\beta_0^{(d)})} - \Im(\beta_0^{(d)})$  to probe the rate of convergence in  $n$ . The bottom panel shows the absolute values  $|\Delta\Re(\beta_0)|$  and  $|\Delta\Im(\beta_0)|$  of the differences as a

function of  $n$ , which appear to decay exponentially. This observation is in line with the fact that the contributions of sub-leading partition function zeros are suppressed with power  $n$ , see Equation (10).

Next, we repeat the same analysis with data for the density of states obtained by MHR of PA data with system size  $L = 16$ . For each value of  $\mathcal{R}$  we carried out an independent simulation. Although reweighting in  $J_2$  is in principle possible, the reweighting range is rather limited. The results of this exercise are shown in Figure 3, and they are found to be qualitatively quite similar to the previous case. As is to be expected, the leading Fisher zero is closer to the real axis as compared to  $L = 4$ . As before, the cumulants are evaluated at  $\beta = \Re(\beta_0^{(d)})$  from the direct method, which is possible thanks to the estimate of the density of states  $\Omega$  from MHR. In particular, the exponential decay of the differences between the cumulant and direct method is more clearly visible in this case. Note that the bottom row only shows the systematic deviation of the two methods when using the same data for  $\Omega(\Sigma_1, \Sigma_2)$  (subject to statistical errors), and not the actual error for  $\beta_0$ . For an estimate of the statistical errors encountered in the simulation, see the error bars in Figure A2. This demonstrates that the cumulant method is a viable replacement for the direct method whenever the statistical error exceeds the systematic deviation shown above (which it typically does). However, it does not say anything about the actual accuracy of the obtained results. Also, note that even on the logarithmic scale, the difference decays monotonously and no noise is visible even when using higher-order cumulants. This is because despite the fact that higher-order cumulants are noisy, the fluctuations in their ratios do not increase noticeably with  $n$ , which is due to the cross-correlation between the terms.

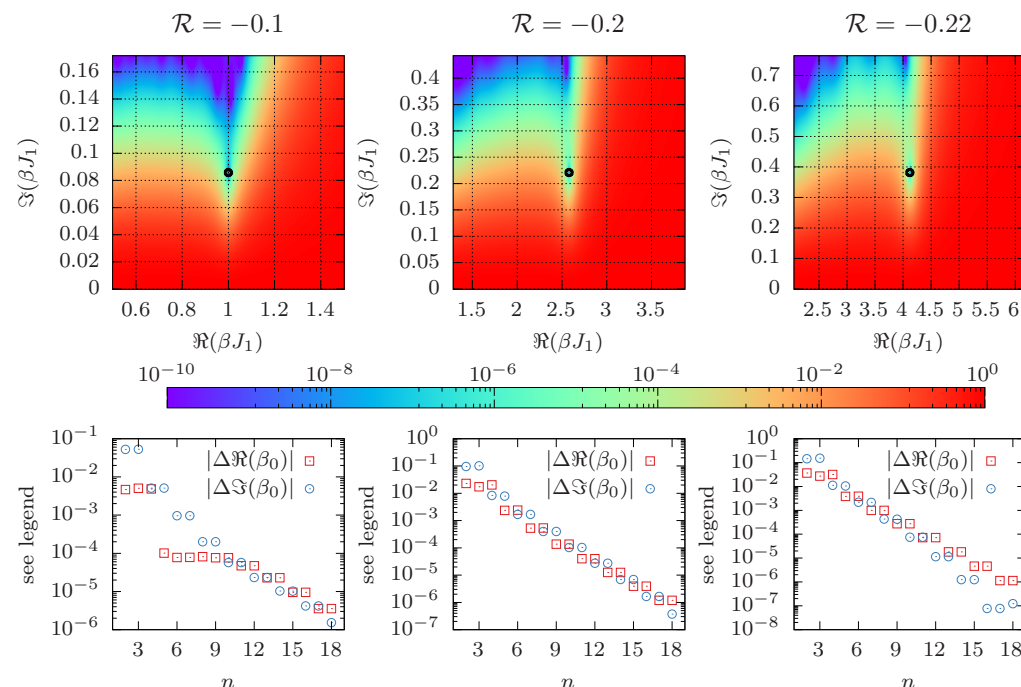


**Figure 3.** Same as Figure 2 for  $L = 16$ , but using PA simulation data instead of exact enumeration.

### 3.3. Determining the Leading Lee–Yang Zero Directly and by the Cumulant Method

We now turn to an analysis of the Lee–Yang zeros. We consider the partition function in the complex-field plane at our best estimate for the infinite-volume critical temperature for different values of  $\mathcal{R}$  (see Section 3.4 for details). Analogous to the Fisher zeros discussed in the previous section, Lee–Yang zeros are obtained using the direct method (utilizing the LM algorithm). As their calculation requires the density of states  $\Omega(\Sigma_1, \Sigma_2, M)$ , we only compute them for  $L = 4$ .

Similar to Figure 2, the top panel of Figure 4 shows the absolute value of the partition function in the complex field plane at the infinite-volume inverse critical temperature  $\beta_c$ , i.e.,  $|Z_{\beta_c}(\Re(h), \Im(h))|$ . The found zeros are consistent with being purely imaginary, suggesting that the Lee–Yang circle theorem may also hold for the model considered here. (Note that we are unaware of any rigorous proof of the circle theorem for the model at hand.) We again also considered the alternative approach provided by the cumulant method, and the bottom panel of Figure 4 depicts the deviation of the estimate of the cumulant method from the zero determined via the direct method as a function of  $n$ . As was the case for the Fisher zeros, the deviation vanishes exponentially in  $n$ . Note that the range of the real part of the external magnetic field is the same in all three panels. For smaller values of  $\mathcal{R}$ , the minimum of  $|Z_{\beta_c}(h)|$  becomes broader, making it more difficult to find the root numerically. The imaginary part of the leading Lee–Yang zero vanishes as  $\mathcal{R}$  approaches  $-1/4$ .

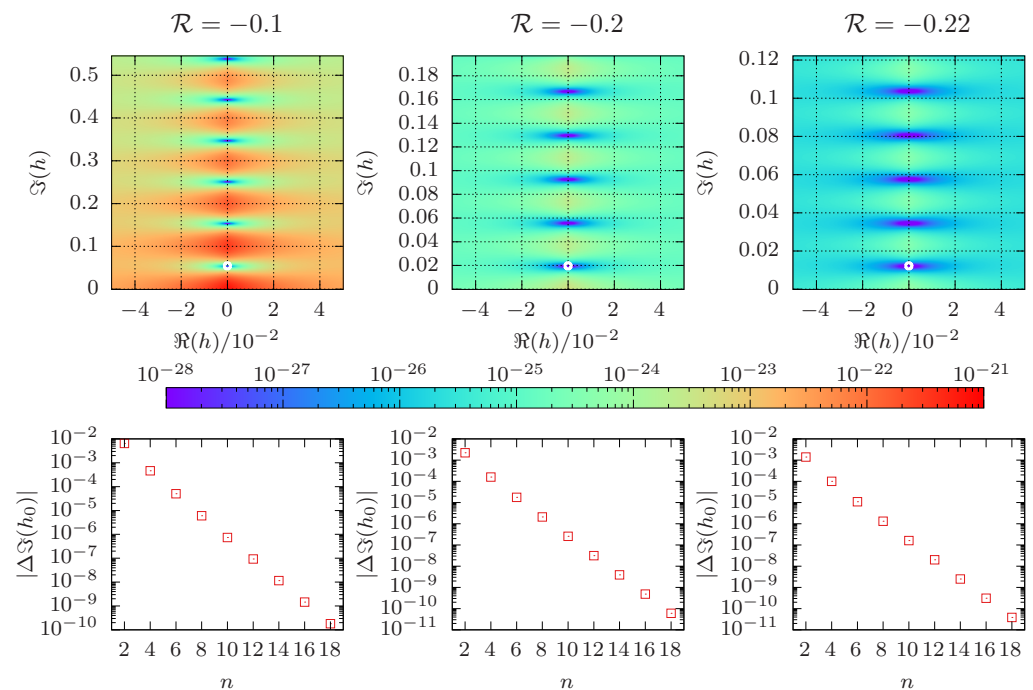


**Figure 4.** The top row shows  $|Z_{\beta_c}(\Re(h), \Im(h))|$  for complex  $h$ , as obtained from Equation (7) for  $\mathcal{R} \in \{-0.1, -0.2, -0.22\}$ , calculated by exact enumeration for  $L = 4$  at  $\beta_c$ . For  $\beta_c$  we used our best estimate, see Section 3.4. The leading Lee–Yang zero is denoted by an open white circle. The bottom row shows the difference in  $\Im(h_0)$  for the approximation given by Equation (13) of order  $n$  and the directly obtained value.

### 3.4. Comparison of Standard FSS and Scaling of Partition Function Zeros

One recently proposed advantage of using the partition function zeros to obtain critical exponents is that already rather small system sizes may yield quite accurate estimates for the exponents [39]. In the following, we present tables for different values of  $\mathcal{R}$  and different fit intervals from  $L_{\min}$  to  $L_{\max}$ , thus clearly demonstrating for which ranges of system sizes reliable FSS fits can be performed. We consider the system sizes  $L \in \{8, 16, 24, 32, 48, 64, 88\}$  and values of  $\mathcal{R}$  equal to  $-0.1, -0.2, -0.21$ , and  $-0.22$ . As the results for  $\mathcal{R} = -0.21$  are analogous to the other values of  $\mathcal{R}$ , they are only included in the Supplementary Materials, and not presented in the main text. For every system size  $L$  and for every value of  $\mathcal{R}$ , ten independent PA runs were carried out in order to improve statistics and to obtain error bars. The first run determined the temperature set for the remaining runs. In principle, the energy histogram overlap defines the temperature set uniquely. However, the actually determined temperatures by PA are subject to statistical fluctuations. Thus, to avoid every realization having its own temperatures, the first run is used to fix the temperature set.

The same simulation data were used for the comparison of standard FSS and the scaling of partition function zeros obtained via the cumulant method using up to the 20-th cumulant (corresponding to  $n = 18$  in Equation (12) for Fisher zeros, and  $k = 9$  in Equation (13) for Lee–Yang zeros). As shown above, we did not observe any loss in numeric precision using higher-order cumulants. Therefore, we use the largest cumulant that we measured; see also Appendix B.

### 3.4.1. Scaling of Fisher Zeros

Table 1 summarizes the FSS results for  $\mathcal{R} = -0.1, -0.2$ , and  $-0.22$  using the leading Fisher zero as well as the logarithmic derivative of the magnetization,

$$d\ln|m| \equiv \frac{\partial}{\partial \beta} \ln\langle|M|\rangle = \frac{\langle|M|\mathcal{H}\rangle}{\langle|M|\rangle} - \langle\mathcal{H}\rangle, \quad (16)$$

whose maximum follows the FSS relation  $d\ln|m|_{\max}(L) \propto L^{y_t}$  [67]. As the precise inverse temperature at which  $\Re(\beta - \beta_0)$  is zero is not in general contained in the annealing schedule of PA, we first determine the zero crossing in the estimate for  $\Re(\beta - \beta_0)$  with positive slope closest to the location of the local maximum of the second energy cumulant (ignoring the  $\beta = 0$  maximum). Next, we determine the  $\beta$  for which the linear interpolation of  $\Re(\beta - \beta_0)$  of Equation (12) between the two closest inverse temperatures is zero.  $\Im(\beta_0)$  is also obtained through linear interpolation to the same  $\beta$  which we found to be more stable than to evaluate  $\Re(\beta_0)$  and  $\Im(\beta_0)$  directly using Equation (12). This is subsequently used for FSS. Details from all fits yielding estimates for  $y_t$  can be found in Section 2.1 of the Supplementary Materials. The expected exponent is the Onsager value,  $y_t = 1$ . The estimates  $y_t^F$  and  $y_t^{d\ln|m|}$  for  $y_t$  resulting from both methods are close to the expected value for the considered ranges of system sizes for all  $\mathcal{R}$ , albeit not always within error bars.

For  $\mathcal{R} = -0.1$  it comes as a surprise that the values from standard FSS using  $d\ln|m|$  are closer to 1 and appear to have weaker corrections to scaling. Specifically, the value obtained for  $y_t^{d\ln|m|}$  is within 0.5% of the expected value for all fit ranges, whereas the value for  $y_t^F$  differs by as much as 3% when using the fitting range 8–24 for  $L$ . While when  $L_{\min} = 8$  the value for  $y_t$  using the leading Fisher zero is far below 1, it is consistent with 1 for larger  $L_{\min}$ , suggestive of the differing value for smaller system sizes being due to stronger corrections to scaling.

In contrast, for  $\mathcal{R} = -0.2$  for almost any (fixed) fitting range the two estimates are compatible with each other within error bars, and the error bars are comparable in magnitude. Most of the  $y_t$  estimates fall well below the expected value  $y_t = 1$ , and increase with both  $L_{\min}$  and  $L_{\max}$ , being compatible with 1 only for fitting ranges limited to the largest system sizes studied here. This effective variation in the exponent with  $L$  is also reflected in the poor quality of fit: In most ranges  $[L_{\min}, L_{\max}]$  the  $Q$  value falls below 0.1 [68], where  $Q$  refers to the probability of drawing a  $\chi^2$  from the  $\chi^2$  distribution that is even larger than the value calculated from the fit. Unusually small values for  $Q$  correspond to poor quality of fit.

For  $\mathcal{R} = -0.22$ , the estimates for  $y_t$  are even further below the Onsager value of  $y_t = 1$ , and again increase with  $L_{\min}$  and  $L_{\max}$ , suggestive of the presence of strong corrections to scaling. Only in the range [48, 88] is the result within error bars of the Onsager value. Here too, the effectively changing exponent is reflected in poor fit qualities. Differently from the previous cases, however, the value for  $y_t$  from the Fisher zeros is consistently closer to the expected value than the value from regular FSS, suggesting that corrections to scaling are weaker for the location of the Fisher zeros in this case. The overall worse fit quality for  $d\ln|m|$  is also in agreement with stronger correction terms.

**Table 1.** Estimates for  $y_t$  from FSS fits using the imaginary part of the leading Fisher zero as well as  $\text{dln}|m|$  for different  $L_{\min}$  and  $L_{\max}$ , and using  $\mathcal{R} = -0.1, -0.2$ , and  $-0.22$ .

$L_{\max}$	24	32	48	64	88
$L_{\min}$					
$\mathcal{R} = -0.1$					
8	$y_t^F = 0.9668(61)$ $y_t^{\text{dln} m } = 0.9957(24)$	$y_t^F = 0.9667(48)$ $y_t^{\text{dln} m } = 0.9943(17)$	$y_t^F = 0.9796(31)^\dagger$ $y_t^{\text{dln} m } = 0.9941(15)$	$y_t^F = 0.9817(29)^\dagger$ $y_t^{\text{dln} m } = 0.9939(13)$	$y_t^F = 0.9829(29)^\dagger$ $y_t^{\text{dln} m } = 0.9941(11)$
16	—	$y_t^F = 0.972(15)$ $y_t^{\text{dln} m } = 0.9867(96)$	$y_t^F = 1.0001(79)^\dagger$ $y_t^{\text{dln} m } = 0.9908(51)$	$y_t^F = 1.0026(70)$ $y_t^{\text{dln} m } = 0.9916(35)$	$y_t^F = 1.0052(68)^\dagger$ $y_t^{\text{dln} m } = 0.9932(23)$
24	—	—	$y_t^F = 1.017(13)$ $y_t^{\text{dln} m } = 0.9908(51)$	$y_t^F = 1.018(11)$ $y_t^{\text{dln} m } = 0.9916(35)$	$y_t^F = 1.022(11)$ $y_t^{\text{dln} m } = 0.9933(23)$
32	—	—	—	$y_t^F = 1.042(21)$ $y_t^{\text{dln} m } = 0.9935(50)$	$y_t^F = 1.049(19)$ $y_t^{\text{dln} m } = 0.9948(31)$
48	—	—	—	—	$y_t^F = 1.048(38)$ $y_t^{\text{dln} m } = 0.9959(65)$
$\mathcal{R} = -0.2$					
8	$y_t^F = 0.9215(35)$ $y_t^{\text{dln} m } = 0.9211(27)^\dagger$	$y_t^F = 0.9263(31)^\dagger$ $y_t^{\text{dln} m } = 0.9284(18)^\dagger$	$y_t^F = 0.9369(26)^\dagger$ $y_t^{\text{dln} m } = 0.9344(15)^\dagger$	$y_t^F = 0.9400(23)^\dagger$ $y_t^{\text{dln} m } = 0.9380(14)^\dagger$	$y_t^F = 0.9453(21)^\dagger$ $y_t^{\text{dln} m } = 0.9484(10)^\dagger$
16	—	$y_t^F = 0.9500(86)$ $y_t^{\text{dln} m } = 0.9493(47)$	$y_t^F = 0.9663(54)^\dagger$ $y_t^{\text{dln} m } = 0.9581(34)^\dagger$	$y_t^F = 0.9639(42)^\dagger$ $y_t^{\text{dln} m } = 0.9625(29)^\dagger$	$y_t^F = 0.9702(37)^\dagger$ $y_t^{\text{dln} m } = 0.9707(19)^\dagger$
24	—	—	$y_t^F = 0.994(12)$ $y_t^{\text{dln} m } = 0.9694(64)^\dagger$	$y_t^F = 0.9780(83)$ $y_t^{\text{dln} m } = 0.9737(48)$	$y_t^F = 0.9872(68)^\dagger$ $y_t^{\text{dln} m } = 0.9788(26)$
32	—	—	—	$y_t^F = 0.968(15)^\dagger$ $y_t^{\text{dln} m } = 0.9829(65)$	$y_t^F = 0.988(11)^\dagger$ $y_t^{\text{dln} m } = 0.9833(32)$
48	—	—	—	—	$y_t^F = 0.990(20)^\dagger$ $y_t^{\text{dln} m } = 0.9838(67)$
$\mathcal{R} = -0.22$					
8	$y_t^F = 0.9328(30)^\dagger$ $y_t^{\text{dln} m } = 0.8781(25)^\dagger$	$y_t^F = 0.9356(23)^\dagger$ $y_t^{\text{dln} m } = 0.8907(19)^\dagger$	$y_t^F = 0.9364(21)^\dagger$ $y_t^{\text{dln} m } = 0.9019(15)^\dagger$	$y_t^F = 0.9410(18)^\dagger$ $y_t^{\text{dln} m } = 0.9112(13)^\dagger$	$y_t^F = 0.9461(15)^\dagger$ $y_t^{\text{dln} m } = 0.9167(12)^\dagger$
16	—	$y_t^F = 0.9525(76)$ $y_t^{\text{dln} m } = 0.9302(42)$	$y_t^F = 0.9513(63)$ $y_t^{\text{dln} m } = 0.9365(28)$	$y_t^F = 0.9588(45)$ $y_t^{\text{dln} m } = 0.9431(22)^\dagger$	$y_t^F = 0.9644(32)$ $y_t^{\text{dln} m } = 0.9484(19)^\dagger$
24	—	—	$y_t^F = 0.948(13)$ $y_t^{\text{dln} m } = 0.9437(54)$	$y_t^F = 0.9634(71)$ $y_t^{\text{dln} m } = 0.9525(36)^\dagger$	$y_t^F = 0.9697(46)$ $y_t^{\text{dln} m } = 0.9600(30)^\dagger$
32	—	—	—	$y_t^F = 0.971(11)$ $y_t^{\text{dln} m } = 0.9612(53)$	$y_t^F = 0.9766(68)$ $y_t^{\text{dln} m } = 0.9702(42)^\dagger$
48	—	—	—	—	$y_t^F = 0.995(16)$ $y_t^{\text{dln} m } = 0.9905(84)$

<sup>†</sup> Q value below 0.1.

### 3.4.2. Scaling of Lee–Yang Zeros

In the following, we obtain  $y_h$  from the scaling behavior (see Equation (5)) of the leading Lee–Yang zero at the (fixed) inverse temperature  $\beta_c$ , as well as from the value of the magnetic susceptibility  $\chi$  at  $\beta_c$ , which follows the scaling relation

$$\chi_L(\beta_c) = L^{-D} \beta_c \langle M^2 \rangle_{\beta_c} \propto L^{-D+2y_h} = L^{\gamma/\nu}, \quad (17)$$

with  $D$  being the spatial dimension. In principle, one may also use the pseudo-critical points of the magnetic susceptibility with subtraction and its peak heights, which follow the same scaling relation. However, as we use the critical temperature for the Lee–Yang zeros, this would result in an unfair comparison and the values from the magnetic susceptibility by design would be subject to stronger corrections to scaling.

We consider the Lee–Yang zeros at our estimate for the inverse critical temperature  $\beta_c$  obtained from the scaling of the real part of the Fisher zeros for the different values of  $\mathcal{R}$ . This estimate is found by applying the fit ansatz  $\Re(\beta_0(L)) = \beta_c - aL^{-y_t} - bL^{-2y_t}$ , allowing for a first-order correction term and assuming  $y_t = 1$ . Using the full range of system sizes, i.e.,  $L = 8, \dots, 88$ , we obtain  $\beta_c J_1 = 1.02350(32), 2.65740(54), 3.25721(42), 4.27017(59)$  for  $\mathcal{R} = -0.1, -0.2, -0.21$ , and  $-0.22$ , respectively (cf. Supplementary Tables S9–S12). The Lee–Yang zeros  $\Im(h_0)$  and the susceptibility  $\chi_L$  together with their statistical errors are then evaluated at this value for  $\beta_c$ . Note that as the critical temperature was calculated a posteriori, we have no data for the cumulants at  $\beta_c$ . In order to estimate the value of the cumulants at  $\beta_c$ , we use Lagrange interpolation between the four inverse temperatures closest to  $\beta_c$ , potentially resulting in a small systematic error. As all realizations use the same temperature set, the effect of this is not accounted for in the quoted error bars. Next, one carries out the FSS analysis on the calculated values for the Lee–Yang zeros and the susceptibility at the obtained  $\beta_c$ . In this process the statistical errors in  $\Im(h_0)$  and  $\chi_L$  are correctly reflected in the statistical error of the critical exponent  $y_h$ , whereas the uncertainty in  $\beta_c$  is not accounted for. To estimate the influence of the error of  $\beta_c$  on the estimate for  $y_h$ , one may repeat this analysis at  $\beta_c - \epsilon(\beta_c)$  and  $\beta_c + \epsilon(\beta_c)$ , with  $\epsilon(\beta_c)$  corresponding to the quoted error bars. This yields estimates  $y_h^{(-)}$  and  $y_h^{(+)}$ , thus giving rise to a second contribution  $|y_h^{(+)} - y_h^{(-)}|/2$  to the error of  $y_h$ . Alternatively, to combine both error contributions in the quoted error bars, we carry out jackknifing [69] over the whole FSS procedure. Specifically, we use ten jackknife blocks (each containing nine out of ten PA simulation runs), for which we then perform the entire analysis, resulting in slightly varying values for the Fisher zeros and the inverse critical temperatures. The Lee–Yang zeros and the magnetic susceptibilities are analyzed at the respective  $\beta_c$  of each jackknife block, and finally, result in different estimates for the exponent  $y_h$ . The final estimates of  $y_h$  quoted in Table 2 and Supplementary Tables S13–S20 are then the plain averages of the jackknife blocks. Their standard errors are calculated via the usual rescaled variance of the jackknife blocks, which accounts for their trivial correlation [69,70]. For further details including results for all fitting parameters, see Sections S2.2 and S2.3 of the Supplementary Materials. We have checked that the jackknife estimates for  $\beta_c J_1$  ( $\beta_c J_1 = 1.02351(22), 2.65740(68), 3.25722(84)$ , and  $4.27017(48)$ ) are in very good agreement with our aforementioned final values.

The expected value for  $y_h$  is the  $D = 2$  Ising value  $y_h = 1.875$ . Table 2 summarizes the FSS results using the leading Lee–Yang zero and the magnetic susceptibility for  $\mathcal{R} = -0.1, -0.2$ , and  $-0.22$ . As before, the results are affected by corrections to scaling reflected in effectively varying exponents that approach the expected value as  $L_{\min}$  and  $L_{\max}$  increase. Both methods yield values for  $y_h$  well compatible with the expected exponent of 1.875.

For  $\mathcal{R} = -0.1$ , the estimate  $y_h^{\text{LY}}$  for  $y_h$  from the scaling of the Lee–Yang zeros even on the smallest range of system sizes, i.e.,  $L \in \{8, 16, 24\}$ , is within two error bars of 1.875, as opposed to the estimate  $y_h^{\chi}$  from the magnetic susceptibility, which is far outside the error margin. This indicates stronger corrections to scaling for the magnetic susceptibility, which is also reflected in the overall poorer quality-of-fit value  $Q$ . Despite the big difference when including the value for  $L = 8$ , for  $L_{\min} > 8$  the value for  $y_h$  from the Lee–Yang zeros is only marginally closer to the Ising value as compared to the results from the scaling of the magnetic susceptibility.

Also, for  $\mathcal{R} = -0.2$  the difference between the methods shows most clearly when including the value for  $L = 8$ . Here, the estimate from the partition function zeros is much closer to the expected one, albeit still not within error bars. When choosing  $L_{\min} = 16$ , the value from the Lee–Yang zeros is always within at most two error bars of the expected value, which is not the case for the value from the magnetic susceptibility. However, this observation may not be significant as both values are within the error bars. For  $L \geq 24$ , both methods yield values compatible with each other and with 1.875. Similarly, for  $\mathcal{R} = -0.22$  the Lee–Yang value for  $y_h$  is much closer to 1.875 (but again not within error bars) than the magnetic susceptibility one when including  $L = 8$ . When excluding the smallest system

size, both methods yield results compatible with the Ising exponent, and both methods appear to perform equally well.

**Table 2.** Jackknife estimates at  $\beta_c$  (see text) for  $y_h$  from FSS fits using the leading Lee–Yang zero as well as from the value of the magnetic susceptibility  $\chi_L$  at  $\beta_c$  for different  $L_{\min}$  and  $L_{\max}$ , and using  $\mathcal{R} = -0.1, -0.2$ , and  $-0.22$ .

$L_{\max}$ $L_{\min}$	24	32	48	64	88
$\mathcal{R} = -0.1$					
8	$y_h^{\text{LY}} = 1.87629(97)$ $y_h^{\chi} = 1.87813(86)$	$y_h^{\text{LY}} = 1.87564(69)$ $y_h^{\chi} = 1.87730(57)^+$	$y_h^{\text{LY}} = 1.8756(13)$ $y_h^{\chi} = 1.8769(11)^+$	$y_h^{\text{LY}} = 1.8754(20)$ $y_h^{\chi} = 1.8764(17)^+$	$y_h^{\text{LY}} = 1.8754(25)$ $y_h^{\chi} = 1.8763(21)^+$
16	–	$y_h^{\text{LY}} = 1.8747(13)$ $y_h^{\chi} = 1.8755(11)^+$	$y_h^{\text{LY}} = 1.8751(23)$ $y_h^{\chi} = 1.8757(20)$	$y_h^{\text{LY}} = 1.8750(30)$ $y_h^{\chi} = 1.8754(26)$	$y_h^{\text{LY}} = 1.8751(35)$ $y_h^{\chi} = 1.8755(31)$
24	–	–	$y_h^{\text{LY}} = 1.8745(38)$ $y_h^{\chi} = 1.8751(34)$	$y_h^{\text{LY}} = 1.8747(42)$ $y_h^{\chi} = 1.8750(37)$	$y_h^{\text{LY}} = 1.8750(46)$ $y_h^{\chi} = 1.8753(40)$
32	–	–	–	$y_h^{\text{LY}} = 1.8758(49)$ $y_h^{\chi} = 1.8759(42)$	$y_h^{\text{LY}} = 1.8757(50)$ $y_h^{\chi} = 1.8759(43)$
48	–	–	–	–	$y_h^{\text{LY}} = 1.8752(49)$ $y_h^{\chi} = 1.8754(43)$
$\mathcal{R} = -0.2$					
8	$y_h^{\text{LY}} = 1.8780(13)$ $y_h^{\chi} = 1.8828(13)^+$	$y_h^{\text{LY}} = 1.8772(16)$ $y_h^{\chi} = 1.8813(14)^+$	$y_h^{\text{LY}} = 1.8771(18)$ $y_h^{\chi} = 1.8805(16)^+$	$y_h^{\text{LY}} = 1.8769(20)$ $y_h^{\chi} = 1.8801(17)^+$	$y_h^{\text{LY}} = 1.8767(30)^+$ $y_h^{\chi} = 1.8789(28)^+$
16	–	$y_h^{\text{LY}} = 1.8750(26)$ $y_h^{\chi} = 1.8767(23)$	$y_h^{\text{LY}} = 1.8757(28)$ $y_h^{\chi} = 1.8767(24)$	$y_h^{\text{LY}} = 1.8757(32)$ $y_h^{\chi} = 1.8765(28)$	$y_h^{\text{LY}} = 1.8759(44)$ $y_h^{\chi} = 1.8763(38)$
24	–	–	$y_h^{\text{LY}} = 1.8759(35)$ $y_h^{\chi} = 1.8761(30)$	$y_h^{\text{LY}} = 1.8757(38)$ $y_h^{\chi} = 1.8759(33)$	$y_h^{\text{LY}} = 1.8760(48)$ $y_h^{\chi} = 1.8761(42)$
32	–	–	–	$y_h^{\text{LY}} = 1.8765(41)$ $y_h^{\chi} = 1.8765(36)$	$y_h^{\text{LY}} = 1.8763(52)$ $y_h^{\chi} = 1.8763(46)$
48	–	–	–	–	$y_h^{\text{LY}} = 1.8758(66)$ $y_h^{\chi} = 1.8759(57)$
$\mathcal{R} = -0.22$					
8	$y_h^{\text{LY}} = 1.88294(89)$ $y_h^{\chi} = 1.88778(65)^+$	$y_h^{\text{LY}} = 1.8818(11)^+$ $y_h^{\chi} = 1.8860(11)^+$	$y_h^{\text{LY}} = 1.8808(12)^+$ $y_h^{\chi} = 1.8845(12)^+$	$y_h^{\text{LY}} = 1.8804(10)^+$ $y_h^{\chi} = 1.88300(95)^+$	$y_h^{\text{LY}} = 1.8803(10)^+$ $y_h^{\chi} = 1.88288(95)^+$
16	–	$y_h^{\text{LY}} = 1.8777(22)$ $y_h^{\chi} = 1.8791(19)$	$y_h^{\text{LY}} = 1.8766(16)$ $y_h^{\chi} = 1.8777(16)$	$y_h^{\text{LY}} = 1.8781(14)$ $y_h^{\chi} = 1.8786(13)$	$y_h^{\text{LY}} = 1.8781(13)$ $y_h^{\chi} = 1.8786(12)$
24	–	–	$y_h^{\text{LY}} = 1.8752(17)$ $y_h^{\chi} = 1.8758(16)$	$y_h^{\text{LY}} = 1.8779(18)$ $y_h^{\chi} = 1.8781(15)$	$y_h^{\text{LY}} = 1.8780(17)$ $y_h^{\chi} = 1.8782(15)$
32	–	–	–	$y_h^{\text{LY}} = 1.8792(23)$ $y_h^{\chi} = 1.8792(19)$	$y_h^{\text{LY}} = 1.8793(21)$ $y_h^{\chi} = 1.8792(18)$
48	–	–	–	–	$y_h^{\text{LY}} = 1.8827(36)$ $y_h^{\chi} = 1.8817(30)$

<sup>†</sup>  $Q$  value below 0.1.

#### 4. Conclusions

We have studied the Fisher and Lee–Yang zeros for the frustrated  $J_1$ – $J_2$  Ising model on the honeycomb lattice. The partition function zeros are obtained using a recently suggested cumulant method [38,48,57,58] that does not require knowledge of the density of states  $\Omega$ . For small systems where  $\Omega$  was available, we compared the values for the leading Fisher and Lee–Yang zeros from the cumulant method against the directly obtained estimates and observed only small deviations that vanish exponentially in the cumulant order  $n$ , regardless of the value of  $\mathcal{R}$ . For larger systems, we also saw an exponential convergence of the cumulant estimates to their asymptotic values when evaluating the cumulants at  $\beta$  close to  $\Re(\beta_0)$ .

We compared FSS using the location of the leading partition function zeros with a traditional FSS protocol. Both approaches indicate that the model remains in the Ising universality class for all studied values of  $\mathcal{R} > -1/4$ . For the temperature exponent  $y_t$ , our numerical results do not favor one method over the other. Instead, both approaches seem to be subject to non-trivial corrections to scaling, such that dependent on  $\mathcal{R}$  one or the other approach appears preferable. For  $\mathcal{R} = -0.1$  conventional FSS shows practically no signs of corrections to scaling even for very small systems, whereas the values obtained for  $y_t$  from the partition function zeros have a clear system-size dependence. On the other hand, for values of  $\mathcal{R}$  closer to  $-1/4$ , conventional FSS is subject to very strong corrections to scaling, whereas the values obtained using the partition function zeros show only slightly stronger corrections as compared to  $\mathcal{R} = -0.1$ . Therefore, our data for the partition function zeros for  $\mathcal{R} = -0.22$  convincingly indicate that the system remains in the Ising universality class, whereas the results from traditional FSS alone are much less conclusive. The field exponent  $y_h$ , as obtained from the Lee–Yang zeros, in most cases was marginally closer to the expected value than the estimate derived from the magnetic susceptibility, although only when including the smallest system size of  $L = 8$  the former approach performed significantly better than the latter.

Thus, based on our results, studying the critical behavior using the partition function zeros does not in general promise to yield results less afflicted by scaling corrections but, as expected, in different regimes one or the other approach might have an edge in this respect. Both techniques (as well as other scaling paradigms) can hence be used with good success in a complementary fashion.

**Supplementary Materials:** The following supporting information can be downloaded at: <https://www.mdpi.com/article/10.3390/e26110919/s1>, it contains a video illustrating the motion of Fisher zeros on varying  $\mathcal{R}$  and tables for the finite-size scaling studies.

**Author Contributions:** Conceptualization, D.G. and W.J.; methodology, D.G.; software, D.G.; validation, W.J. and M.W.; formal analysis, D.G.; writing—original draft preparation, D.G.; writing—review and editing, M.W. and W.J.; visualization, D.G.; supervision, M.W. and W.J.; project administration, W.J.; funding acquisition, W.J. All authors have read and agreed to the published version of the manuscript.

**Funding:** This project was supported by the Deutsch-Französische Hochschule (DFH-UFA) through the Doctoral College “ $\mathbb{L}^4$ ” under Grant No. CDFA-02-07. We further acknowledge the resources provided by the Leipzig Graduate School of Natural Sciences “BuildMoNa”.

**Data Availability Statement:** The data that support the findings of this study are available from the corresponding author upon reasonable request.

**Acknowledgments:** We thank Leïla Moueddene for interesting discussions. This work is dedicated to the memory of Ralph Kenna who passed away at the end of October 2023. Ralph was fascinated by partition function zeros since his PhD Thesis work [54,55] and revisited this versatile tool for obtaining properties of phase transitions during his scientific career many times [39]. We will remember Ralph as good friend and inspiring collaborator. His deep insights, witty comments, and captivating presentations will be dearly missed.

**Conflicts of Interest:** The authors declare no conflicts of interest. The funders had no role in the design of the study; in the collection, analyses, or interpretation of data; in the writing of the manuscript; or in the decision to publish the results.

## Abbreviations

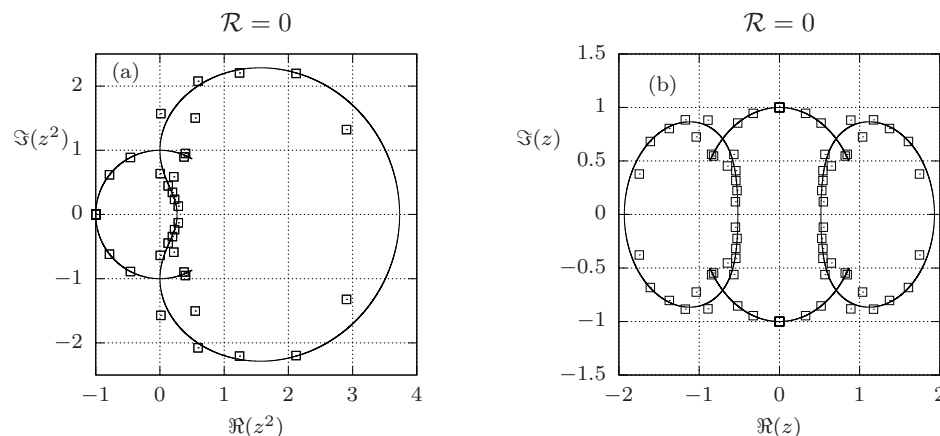
The following abbreviations are used in this manuscript:

MC	Monte Carlo
PA	Population annealing
LY	Lee–Yang
F	Fisher
FSS	Finite-size scaling
RG	Renormalization group

## Appendix A. Fisher Zeros for $\mathcal{R} = 0$

As a consistency check, we carried out the partition function zero analysis for  $\mathcal{R} = 0$  in the complex temperature plane, where exact Fisher zeros are known in the thermodynamic limit [71,72]. The Fisher zeros of the field-free Ising model on the honeycomb lattice without next-nearest-neighbor interactions lie on the partial circle  $z^2 = e^{i\varphi}$  for  $\varphi \in [\pi/3, 5\pi/3]$ , and the heart-shape-like curve given by [72]

$$\left[ \Im(z^2) \right]^2 = 1 + 2\Re(z^2) - \left[ \Re(z^2) \right]^2 \pm \sqrt{8\Re(z^2)}. \quad (\text{A1})$$



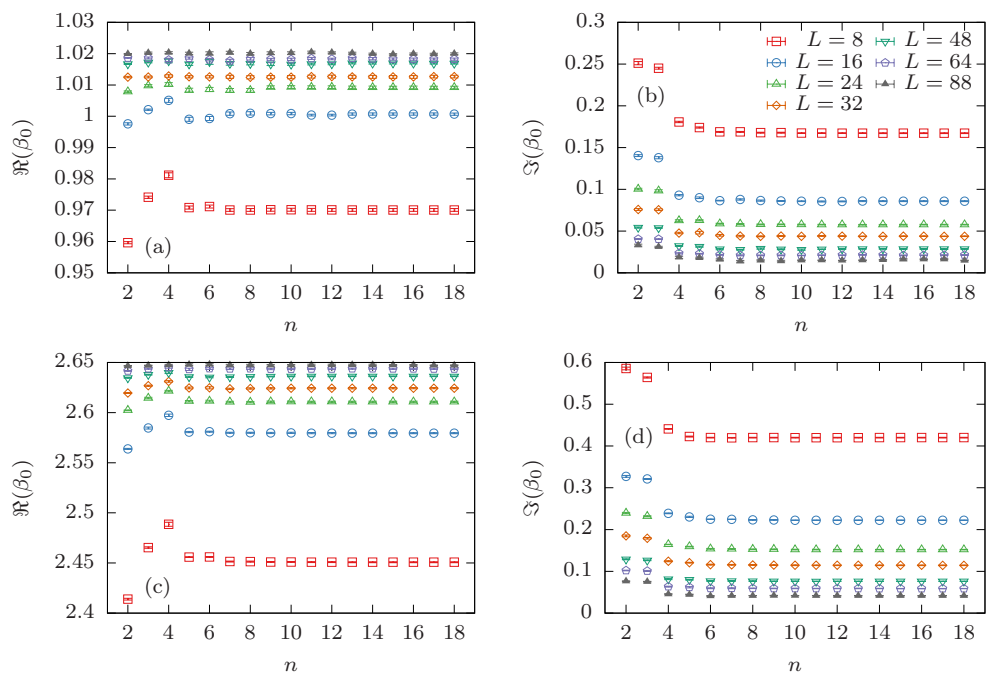
**Figure A1.** Fisher zeros in the complex temperature planes (a)  $z^2 = e^{-2\beta J_1}$  and (b)  $z = e^{-\beta J_1}$  for  $\mathcal{R} = 0$ . Points denote our data for  $L = 4$  obtained by exact enumeration. The solid lines are the exact zeros for  $L \rightarrow \infty$  [71,72].

Figure A1 shows the Fisher zeros for  $L = 4$  (points) and for  $L \rightarrow \infty$  (solid lines). Despite the rather small system size, both appear to be already somewhat compatible, with the closest zero for the finite system size, of course, not being located on the positive real axis. As in the absence of next-nearest-neighbor interactions, the partition function is an even polynomial in  $z$ , the natural variable to consider the Fisher zeros is  $z^2$  [see panel (a)]. When using  $z$  as variable, the  $z \rightarrow -z$  symmetry is visible [see panel (b)], which was absent for  $\mathcal{R} \neq 0$ ; cf. Figure 1.

## Appendix B. Convergence of the Cumulant Method for Larger System Sizes

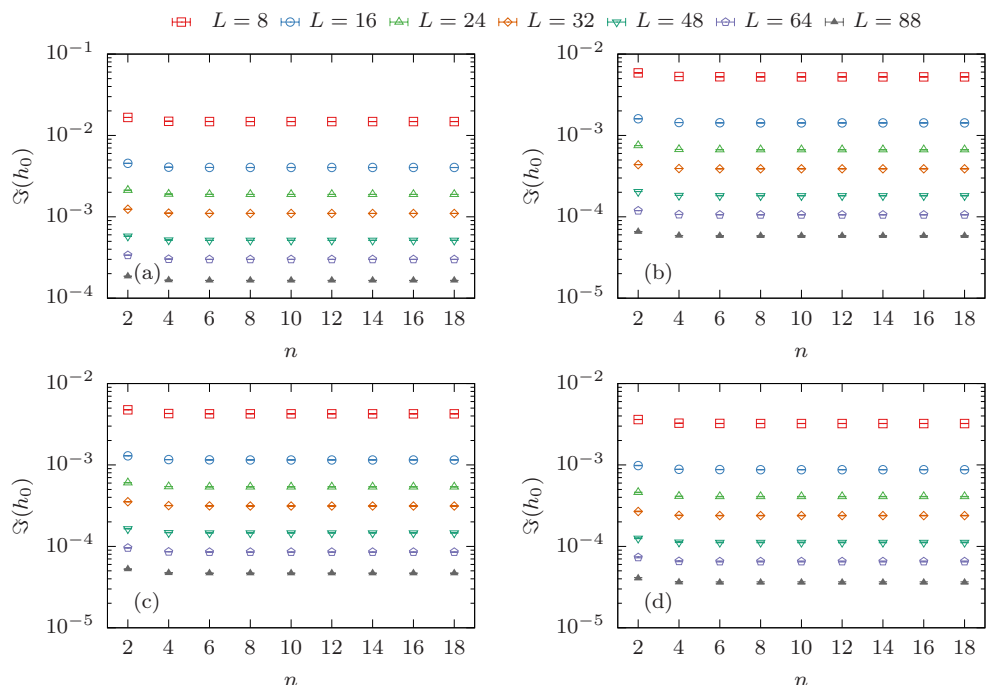
We have tested the convergence of the cumulant method for small system sizes extensively to assure its convergence. For larger system sizes we did not have access to the density of states. To test the convergence for these larger system sizes, we therefore consider the predicted value of the partition function zero as a function of cumulant order  $n$ .

Figure A2 shows the estimated location of the Fisher zero using the cumulant method. The  $\beta_0$  is found by determining the zero crossing of  $\Re(\beta - \beta_0)$ , and the imaginary part is calculated using the equation for  $|\beta - \beta_0|^2$  at that value for  $\beta$ . For all system sizes and for all considered choices of  $\mathcal{R}$ , the estimated value from the cumulant method quickly approaches a constant with increasing  $n$ .



**Figure A2.** Real and imaginary parts of the Fisher zeros  $\beta_0$  obtained through the cumulant method as a function of  $n$  [see Equation (12)] for different  $L$ . In (a,b)  $\mathcal{R} = -0.1$ , and in (c,d)  $\mathcal{R} = -0.2$ .

Similarly, in Figure A3 we show the values for the complex field  $h_0$  of the Lee–Yang zeros at  $\beta_c$  estimated by the cumulant method for the different values of  $\mathcal{R}$  as a function of  $n$ . These also converge quickly. Note that even on the logarithmic scale of Figure A3, error bars do not appear to grow significantly as the order of cumulants is increased. As mentioned above, we attribute this to the fact that despite increasing statistical errors of the individual cumulants, their ratios show only little statistical fluctuation due to the cross-correlation between the terms.



**Figure A3.** Imaginary part of the Lee–Yang zeros  $h_0$  for different system sizes  $L$  and coupling strengths  $\mathcal{R}$ . (a)  $\mathcal{R} = -0.1$ , (b)  $\mathcal{R} = -0.2$ , (c)  $\mathcal{R} = -0.21$ , and (d)  $\mathcal{R} = -0.22$ .

## References

1. Diep, H.T. (Ed.) *Frustrated Spin Systems*, 2nd ed.; World Scientific: Singapore, 2013. [\[CrossRef\]](#)
2. Azaria, P.; Diep, H.T.; Giacomini, H. Coexistence of order and disorder and reentrance in an exactly solvable model. *Phys. Rev. Lett.* **1987**, *59*, 1629–1632. [\[CrossRef\]](#) [\[PubMed\]](#)
3. Espriu, D.; Prats, A. Dynamics of the two-dimensional gonihedric spin model. *Phys. Rev. E* **2004**, *70*, 046117. [\[CrossRef\]](#) [\[PubMed\]](#)
4. Mueller, M.; Johnston, D.A.; Janke, W. Multicanonical analysis of the plaquette-only gonihedric Ising model and its dual. *Nucl. Phys. B* **2014**, *888*, 214–235. [\[CrossRef\]](#)
5. Nightingale, M. Non-universality for Ising-like spin systems. *Phys. Lett. A* **1977**, *59*, 486–488. [\[CrossRef\]](#)
6. Jin, S.; Sen, A.; Sandvik, A.W. Ashkin-Teller criticality and pseudo-first-order behavior in a frustrated Ising model on the square lattice. *Phys. Rev. Lett.* **2012**, *108*, 045702. [\[CrossRef\]](#)
7. Kalz, A.; Honecker, A.; Moliner, M. Analysis of the phase transition for the Ising model on the frustrated square lattice. *Phys. Rev. B* **2011**, *84*, 174407. [\[CrossRef\]](#)
8. Kalz, A.; Honecker, A. Location of the Potts-critical end point in the frustrated Ising model on the square lattice. *Phys. Rev. B* **2012**, *86*, 134410. [\[CrossRef\]](#)
9. Yoshiyama, K.; Hukushima, K. Higher-order tensor renormalization group study of the  $J_1$ - $J_2$  Ising model on a square lattice. *Phys. Rev. E* **2023**, *108*, 054124. [\[CrossRef\]](#)
10. Bobák, A.; Lučivjanský, T.; Žukovič, M.; Borovský, M.; Balcerzak, T. Tricritical behaviour of the frustrated Ising antiferromagnet on the honeycomb lattice. *Phys. Lett. A* **2016**, *380*, 2693–2697. [\[CrossRef\]](#)
11. Acevedo, S.; Arlego, M.; Lamas, C.A. Phase diagram study of a two-dimensional frustrated antiferromagnet via unsupervised machine learning. *Phys. Rev. B* **2021**, *103*, 134422. [\[CrossRef\]](#)
12. Žukovič, M. Critical properties of the frustrated Ising model on a honeycomb lattice: A Monte Carlo study. *Phys. Lett. A* **2021**, *404*, 127405. [\[CrossRef\]](#)
13. Schmidt, M.; Godoy, P. Phase transitions in the Ising antiferromagnet on the frustrated honeycomb lattice. *J. Magn. Magn. Mater.* **2021**, *537*, 168151. [\[CrossRef\]](#)
14. Janke, W. (Ed.) *Rugged Free Energy Landscapes—Common Computational Approaches to Spin Glasses, Structural Glasses and Biological Macromolecules*; Lecture Notes in Physics; Springer: Berlin/Heidelberg, Germany, 2007; Volume 736. [\[CrossRef\]](#)
15. Iba, Y. Population Monte Carlo algorithms. *Trans. Jpn. Soc. Artif. Intell.* **2001**, *16*, 279–286. [\[CrossRef\]](#)
16. Hukushima, K.; Iba, Y. Population annealing and its application to a spin glass. *AIP Conf. Proc.* **2003**, *690*, 200–206. [\[CrossRef\]](#)
17. Machta, J. Population annealing with weighted averages: A Monte Carlo method for rough free-energy landscapes. *Phys. Rev. E* **2010**, *82*, 026704. [\[CrossRef\]](#)
18. Wang, W.; Machta, J.; Katzgraber, H.G. Population annealing: Theory and application in spin glasses. *Phys. Rev. E* **2015**, *92*, 063307. [\[CrossRef\]](#)
19. Christiansen, H.; Weigel, M.; Janke, W. Accelerating molecular dynamics simulations with population annealing. *Phys. Rev. Lett.* **2019**, *122*, 060602. [\[CrossRef\]](#)
20. Rose, N.; Machta, J. Equilibrium microcanonical annealing for first-order phase transitions. *Phys. Rev. E* **2019**, *100*, 063304. [\[CrossRef\]](#)
21. Yang, C.N.; Lee, T.D. Statistical theory of equations of state and phase transitions. I. Theory of condensation. *Phys. Rev.* **1952**, *87*, 404–409. [\[CrossRef\]](#)
22. Lee, T.D.; Yang, C.N. Statistical theory of equations of state and phase transitions. II. Lattice gas and Ising model. *Phys. Rev.* **1952**, *87*, 410–419. [\[CrossRef\]](#)
23. Fisher, M.E. The nature of critical points. In *Lecture Notes in Theoretical Physics*; University of Colorado Press: Boulder, CO, USA, 1965; Volume VII C.
24. Janke, W.; Kenna, R. The strength of first and second order phase transitions from partition function zeroes. *J. Stat. Phys.* **2001**, *102*, 1211–1227. [\[CrossRef\]](#)
25. Janke, W.; Kenna, R. Analysis of the density of partition function zeroes: A measure for phase transition strength. In *Computer Simulation Studies in Condensed-Matter Physics XIV*; Landau, D.P., Lewis, S.P., Schüttler, H.B., Eds.; Springer: Berlin/Heidelberg, Germany, 2002; pp. 97–101. [\[CrossRef\]](#)
26. Janke, W.; Kenna, R. Density of partition function zeroes and phase transition strength. *Comput. Phys. Commun.* **2002**, *147*, 443–446. [\[CrossRef\]](#)
27. Janke, W.; Kenna, R. Phase transition strengths from the density of partition function zeroes. *Nucl. Phys. B Proc. Suppl.* **2002**, *106–107*, 905–907. [\[CrossRef\]](#)
28. Janke, W.; Kenna, R. Finite-size scaling and corrections in the Ising model with Brascamp-Kunz boundary conditions. *Phys. Rev. B* **2002**, *65*, 064110. [\[CrossRef\]](#)
29. Janke, W.; Kenna, R. Exact finite-size scaling with corrections in the two-dimensional Ising model with special boundary conditions. *Nucl. Phys. B Proc. Suppl.* **2002**, *106–107*, 929–931. [\[CrossRef\]](#)
30. Janke, W.; Johnston, D.A.; Kenna, R. New methods to measure phase transition strength. *Nucl. Phys. B Proc. Suppl.* **2003**, *119*, 882–884. [\[CrossRef\]](#)
31. Janke, W.; Johnston, D.A.; Kenna, R. Phase transition strength through densities of general distributions of zeroes. *Nucl. Phys. B* **2004**, *682*, 618–634. [\[CrossRef\]](#)

32. Janke, W.; Johnston, D.A.; Kenna, R. Critical exponents from general distributions of zeroes. *Comput. Phys. Commun.* **2005**, *169*, 457–461. [\[CrossRef\]](#)

33. Janke, W.; Johnston, D.A.; Kenna, R. Properties of phase transitions of higher-order. *PoS (LAT2005)* **2005**, *244*. [\[CrossRef\]](#)

34. Janke, W.; Johnston, D.A.; Kenna, R. Properties of higher-order phase transitions. *Nucl. Phys. B* **2006**, *736*, 319–328. [\[CrossRef\]](#)

35. Kenna, R.; Johnston, D.A.; Janke, W. Scaling relations for logarithmic corrections. *Phys. Rev. Lett.* **2006**, *96*, 115701. [\[CrossRef\]](#) [\[PubMed\]](#)

36. Kenna, R.; Johnston, D.A.; Janke, W. Self-consistent scaling theory for logarithmic-correction exponents. *Phys. Rev. Lett.* **2006**, *97*, 155702. [\[CrossRef\]](#) [\[PubMed\]](#)

37. Moueddeene, L.; Donoso, A.; Berche, B. Ralph Kenna’s scaling relations in critical phenomena. *Entropy* **2024**, *26*, 221. [\[CrossRef\]](#) [\[PubMed\]](#)

38. Deger, A.; Flindt, C. Determination of universal critical exponents using Lee-Yang theory. *Phys. Rev. Res.* **2019**, *1*, 023004. [\[CrossRef\]](#)

39. Moueddeene, L.; G Fytas, N.; Holovatch, Y.; Kenna, R.; Berche, B. Critical and tricritical singularities from small-scale Monte Carlo simulations: The Blume-Capel model in two dimensions. *J. Stat. Mech. Theory Exp.* **2024**, *2024*, 023206. [\[CrossRef\]](#)

40. Monroe, J.L.; Kim, S.Y. Phase diagram and critical exponent  $\nu$  for the nearest-neighbor and next-nearest-neighbor interaction Ising model. *Phys. Rev. E* **2007**, *76*, 021123. [\[CrossRef\]](#)

41. Kim, S.Y. Ising antiferromagnet on a finite triangular lattice with free boundary conditions. *J. Korean Phys. Soc.* **2015**, *67*, 1517–1523. [\[CrossRef\]](#)

42. Sarkanych, P.; Holovatch, Y.; Kenna, R. On the phase diagram of the 2d Ising model with frustrating dipole interaction. *Ukr. J. Phys.* **2015**, *60*, 334–338. [\[CrossRef\]](#)

43. Kim, S.Y. Study of the frustrated Ising model on a square lattice based on the exact density of states. *J. Korean Phys. Soc.* **2021**, *79*, 894–902. [\[CrossRef\]](#)

44. Peng, X.; Zhou, H.; Wei, B.B.; Cui, J.; Du, J.; Liu, R.B. Experimental observation of Lee-Yang zeros. *Phys. Rev. Lett.* **2015**, *114*, 010601. [\[CrossRef\]](#)

45. Ananikian, N.; Kenna, R. Imaginary magnetic fields in the real world. *Physics* **2015**, *8*, 2. [\[CrossRef\]](#)

46. Fläschner, N.; Vogel, D.; Tarnowski, M.; Rem, B.; Lühmann, D.S.; Heyl, M.; Budich, J.; Mathey, L.; Sengstock, K.; Weitenberg, C. Observation of dynamical vortices after quenches in a system with topology. *Nat. Phys.* **2018**, *14*, 265–268. [\[CrossRef\]](#)

47. Macêdo, A.R.S.; Vasilopoulos, A.; Akritidis, M.; Plascak, J.A.; Fytas, N.G.; Weigel, M. Two-dimensional dilute Baxter-Wu model: Transition order and universality. *Phys. Rev. E* **2023**, *108*, 024140. [\[CrossRef\]](#)

48. Flindt, C.; Garrahan, J.P. Trajectory phase transitions, Lee-Yang zeros, and high-order cumulants in full counting statistics. *Phys. Rev. Lett.* **2013**, *110*, 050601. [\[CrossRef\]](#)

49. Itzykson, C.; Pearson, R.B.; Zuber, J.B. Distribution of zeros in Ising and gauge models. *Nucl. Phys. B* **1983**, *220*, 415–433. [\[CrossRef\]](#)

50. Bena, I.; Droz, M.; Lipowski, A. Statistical mechanics of equilibrium and nonequilibrium phase transitions: The Yang–Lee formalism. *Int. J. Mod. Phys. B* **2005**, *19*, 4269–4329. [\[CrossRef\]](#)

51. Fröhlich, J.; Rodriguez, P.F. Some applications of the Lee-Yang theorem. *J. Math. Phys.* **2012**, *53*, 095218. [\[CrossRef\]](#)

52. Krasnytska, M.; Berche, B.; Holovatch, Y.; Kenna, R. Violation of Lee-Yang circle theorem for Ising phase transitions on complex networks. *Europhys. Lett.* **2015**, *111*, 60009. [\[CrossRef\]](#)

53. Katsura, S.; Abe, Y.; Yamamoto, M. Distribution of zeros of the partition function of the Ising model. *J. Phys. Soc. Jpn.* **1971**, *30*, 347–357. [\[CrossRef\]](#)

54. Kenna, R.; Lang, C. Finite size scaling and the zeroes of the partition function in the  $\Phi_4^4$  model. *Phys. Lett. B* **1991**, *264*, 396–400. [\[CrossRef\]](#)

55. Kenna, R.; Lang, C.B. Scaling and density of Lee-Yang zeros in the four-dimensional Ising model. *Phys. Rev. E* **1994**, *49*, 5012–5017. [\[CrossRef\]](#) [\[PubMed\]](#)

56. Hong, S.; Kim, D.H. Logarithmic finite-size scaling correction to the leading Fisher zeros in the  $p$ -state clock model: A higher-order tensor renormalization group study. *Phys. Rev. E* **2020**, *101*, 012124. [\[CrossRef\]](#) [\[PubMed\]](#)

57. Deger, A.; Brandner, K.; Flindt, C. Lee-Yang zeros and large-deviation statistics of a molecular zipper. *Phys. Rev. E* **2018**, *97*, 012115. [\[CrossRef\]](#)

58. Deger, A.; Flindt, C. Lee-Yang theory of the Curie-Weiss model and its rare fluctuations. *Phys. Rev. Res.* **2020**, *2*, 033009. [\[CrossRef\]](#)

59. Deger, A.; Brange, F.; Flindt, C. Lee-Yang theory, high cumulants, and large-deviation statistics of the magnetization in the Ising model. *Phys. Rev. B* **2020**, *102*, 174418. [\[CrossRef\]](#)

60. Janke, W.; Kappler, S. Monte-Carlo study of pure-phase cumulants of 2D  $q$ -state Potts models. *J. Phys. I* **1997**, *7*, 663–674. [:1997183](#) [\[CrossRef\]](#)

61. Gessert, D.; Janke, W.; Weigel, M. Resampling schemes in population annealing—Numerical and theoretical results. *Phys. Rev. E* **2023**, *108*, 065309. [\[CrossRef\]](#)

62. Weigel, M.; Barash, L.; Shchur, L.; Janke, W. Understanding population annealing Monte Carlo simulations. *Phys. Rev. E* **2021**, *103*, 053301. [\[CrossRef\]](#)

63. Barash, L.Y.; Weigel, M.; Borovský, M.; Janke, W.; Shchur, L.N. GPU accelerated population annealing algorithm. *Comput. Phys. Commun.* **2017**, *220*, 341–350. [[CrossRef](#)]
64. Gessert, D.; Janke, W.; Weigel, M. (in preparation).
65. Levenberg, K. A method for the solution of certain non-linear problems in least squares. *Q. Appl. Math.* **1944**, *2*, 164–168. [[CrossRef](#)]
66. Marquardt, D.W. An algorithm for least-squares estimation of nonlinear parameters. *J. Soc. Ind. Appl. Math.* **1963**, *11*, 431–441. [[CrossRef](#)]
67. Ferrenberg, A.M.; Landau, D.P. Critical behavior of the three-dimensional Ising model: A high-resolution Monte Carlo study. *Phys. Rev. B* **1991**, *44*, 5081–5091. [[CrossRef](#)] [[PubMed](#)]
68. Press, W.H.; Teukolsky, S.A.; Vetterling, W.T.; Flannery, B.P. *Numerical Recipes*; Cambridge University Press: New York, NY, USA, 2007.
69. Efron, B. *The Jackknife, the Bootstrap, and Other Resampling Plans*; Society for Industrial and Applied Mathematics: Philadelphia, PA, USA, 1982. [[CrossRef](#)]
70. Janke, W. Monte Carlo Simulations in Statistical Physics—From Basic Principles to Advanced Applications. In *Order, Disorder and Criticality*; Holovatch, Y., Ed.; World Scientific: Singapore, 2012; pp. 93–166. [[CrossRef](#)]
71. Matveev, V.; Shrock, R. Complex-temperature singularities in the  $d = 2$  Ising model: Triangular and honeycomb lattices. *J. Phys. A* **1996**, *29*, 803–823. [[CrossRef](#)]
72. Kim, S.Y.; Hwang, C.O.; Kim, J.M. Partition function zeros of the antiferromagnetic Ising model on triangular lattice in the complex temperature plane for nonzero magnetic field. *Nucl. Phys. B* **2008**, *805*, 441–450. [[CrossRef](#)]

**Disclaimer/Publisher’s Note:** The statements, opinions and data contained in all publications are solely those of the individual author(s) and contributor(s) and not of MDPI and/or the editor(s). MDPI and/or the editor(s) disclaim responsibility for any injury to people or property resulting from any ideas, methods, instructions or products referred to in the content.